PAPER

Check for updates

Significant electrochemical performance improvement of an anion MOF-based solid-state electrolyte across a wide temperature range *via* an ion exchange strategy

Changqi Gu, Wenyu Ding, Sheng Jin, Xinyu Tang, Xin Zhang, Li Fan, Zhiliang Liu [ID] and Xiaomin Kang [ID] *

Low ionic conductivity (σ) and high activation energy (E_a) seriously hinder the development of solid-state electrolytes (SSEs). Herein, a series of post-modified Li$^+$@Ni-MOF-X (X = 1, 2, and 3) materials were synthesized *via* an ion exchange method based on a 3D anionic trinuclear cluster-based metal–organic framework (MOF) (Ni-MOF: {[H$_2$N(CH$_3$)$_2$]$_2$[Ni$_3$(μ_3-O) (XN)(BDC)$_3$]·6DMF}$_n$). Compared with the pristine Ni-MOF, Li$^+$@Ni-MOF-2 exhibited significantly enhanced performance as SSEs, featuring a higher σ of 1.28 × 10^{-3} S cm^{-1}, a larger lithium-ion transference number (t_{Li^+}) of 0.76, and a wider electrochemical stability window (ESW) of 5.3 V at room temperature (Ni-MOF: 2.19 × 10^{-4} S cm^{-1}, 0.57, and 5.0 V). Notably, Li$^+$@Ni-MOF-2 maintained excellent σ even at −40 °C (2.12 × 10^{-4} S cm^{-1}) and exhibited an ultra-low E_a (0.08 eV) from 10 to 100 °C, demonstrating potential practical application over a wide temperature range. Moreover, LiFePO$_4$|Li$^+$@Ni-MOF-2|Li full cells stably cycled for 150 cycles at 0.1 C with a capacity retention of 81.30%. This work has enriched the types of MOF-based SSEs, providing the possibility for the application of lithium-ion SSEs in a wide temperature range.

Introduction

Lithium metal batteries (LMBs) have been widely used in various scenarios due to their lowest electrochemical redox potential (−3.04 V), low mass density (0.534 g cm^{-3}), and high theoretical capacity density (3860 mAh g^{-1}).[1–3] Thereinto, electrolyte, as a key member of batteries, has a non-negligible position. Commercial lithium-battery liquid electrolytes (LEs) are gradually being abandoned due to their limitations of easy leakage, flammability and explosive nature.[4,5] In comparison, solid-state electrolytes (SSEs) with high safety and high energy density stand out in practical applications.[6–8] SSEs can be mainly classified into solid inorganic electrolytes (SIEs) and polymer electrolytes (SPEs). For SIEs, although they always own high ionic conductivity (σ) (>0.1 mS cm^{-1}), the poor interfacial compatibility with the electrode material and slow charge transfer at the interface will hinder their development.[9,10] On the contrary, SPEs present excellent mechanical properties, certain flexibility and better interfacial wettability than SIEs, resulting in a reduction in the resistance generated by the polarization during the battery charge/discharge cycle.

However, low σ and lithium ion transference number (t_{Li^+}) seriously reduce the comprehensive performance of SPEs.[11,12] Thus, it is particularly important and necessary to develop some effective SSE materials with satisfactory σ, high t_{Li^+}, low activation energy (E_a) and good interfacial compatibility.

Metal–organic frameworks (MOFs), as a class of porous inorganic–organic hybrid materials, consist of metal ions/clusters and organic ligands,[13–18] which are widely used in the fields of fluorescence recognition,[19] catalysis,[20] supercapacitors,[21] gas adsorption and separation,[22] and electromagnetic wave absorption due to their attractive architecture and unique performance.[23] In particular, they demonstrated significant advantages in the application of lithium-ion SSEs in view of their high specific surface areas, adjustable pore sizes, abundant unsaturated metal active sites and characteristic functional groups.[24] Nevertheless, pristine MOF materials often fail to simultaneously meet the multifaceted application requirements. Fu *et al.* have evaluated the electrochemical performances of a ZIF-8 material, demonstrating a σ value of 4.89 × 10^{-4} S cm^{-1} and t_{Li^+} of 0.66.[25] The σ and t_{Li^+} of HKUST-1 SSE have been measured by Liu *et al.*, showing values of 4.10 × 10^{-4} S cm^{-1} and 0.40, respectively.[26] Moreover, UiO-66 exhibited a low σ value of 3.20 × 10^{-4} S cm^{-1}, low t_{Li^+} of 0.48, and high activation energy (E_a) of 0.43 eV.[27] Up to now, a variety of functional modification strategies have been employed to

College of Chemistry and Chemical Engineering, Inner Mongolia University, Hohhot 010021, P.R. China. E-mail: kangxm@imu.edu.cn

obtain efficient MOF-based composite SSEs and improve the comprehensive electrochemical performance. For example, Li *et al.*[28] prepared MOF-based composites (PVDF-HFP) through the penetration of polymer chains into MOF materials, achieving a large t_{Li^+} (0.6) and high σ (9.5 × 10^{-4} S cm^{-1}). Zhou *et al.*[29] acquired a PL-MIL-125-Li composite SSE with a σ of 3.9 × 10^{-4} S cm^{-1} and electrochemical stability window (ESW) of 4.9 V by using a two-step post-retouching process of lithium ionic liquid (Li-IL) encapsulation and PVDF-LiTFSI introduction. Bruce Dunn *et al.*[30] employed the method for anion fixation at unsaturated metal sites to promote the migration of lithium ions to improve the electrochemical property (1.22 × 10^{-3} S cm^{-1} and 0.21 eV). Huang *et al.*[31] constructed a composite by utilizing soft multicationic oligomers to graft onto a rigid anionic MOF, achieving evident improvements for comprehensive performance (8.7 × 10^{-4} S cm^{-1}, 0.75 and 4.9 V). Although many MOF-based SSEs materials have been reported, the investigations of their electrochemical properties over a wide temperature range, especially at low temperature, are relatively rare. Moreover, a high E_a value is a key influencing factor for limiting reaction kinetics. Therefore, the controllable construction of efficient SSEs with excellent overall capacity across a wide temperature range is both significant and challenging.

In this contribution, a 3D porous cluster-based anionic MOF (Ni-MOF) with $(CH_3)_2NH_2^+$ as a counter cation has been synthesized and characterized as SSE, featuring σ of 2.19 × 10^{-4} S cm^{-1}, t_{Li^+} of 0.57 and ESW of 5.0 V. In order to realize the enhancement of the comprehensive electrochemical performances, a simple and effective cation exchange strategy between Li$^+$ and $(CH_3)_2NH_2^+$ has been employed to form Li$^+$@Ni-MOF-X (X = 1, 2 and 3) SSE candidates. The increase and uniform distribution of the Li$^+$ concentration in the cage cavity after ion exchange will effectively optimize the Li$^+$ transport path, and significantly improve the Li$^+$ transport efficiency by single-ion hopping mechanism.[32] Especially, Li$^+$@Ni-MOF-2 treated by ion exchange for two days exhibits a higher σ (1.28 × 10^{-3} S cm^{-1}), larger t_{Li^+} (0.76), and wider ESW (5.3 V) than Ni-MOF at room temperature, in addition to an exciting σ of 2.12 × 10^{-4} S cm^{-1} at ultra-low temperature (−40 °C). Notably, the low E_a of 0.08 eV across the temperature range of 10 to 100 °C can be calculated, which is in the forefront of previous related reports. More importantly, Li$^+$@Ni-MOF-2 as SSE can be stabilized in the air for 140 days with basically unchanged electrochemical properties. This work provides an effective means for boosting the performance of SSEs, creating more possibilities for practical applications within a wide temperature range.

Experimental section

Materials and methods

All chemicals and solvents used in this work were purchased and used as received without further purification. The reagents included nickel(II) chloride hexahydrate (NiCl$_2$·6H$_2$O, 99.95%), lithium nitrate (LiNO$_3$, 99%), 1,4-benzenedicarboxylic acid

(H$_2$BDC, 99%), 6″-(pyridine-4-yl)-4,2″:4″,4‴-terpyridine (XN), *N,N*-dime-thylformamide (DMF, ≥99.5%), 1 M LiPF$_6$ in ethylene carbonate/diethyl carbonate (EC/DEC, 1 : 1 vol%), anhydrous ethanol (EtOH, ≥99.7%), isopropyl alcohol (IPA, ≥99.7%), polyvinylidene fluoride (PVDF, 99%), poly (tetrafluoroethylene) (PTFE, 60%), *N*-methyl-2-pyrrolidone (NMP, 98%), acetylene black (AB), LiFePO$_4$, CR2032 coin cell components, and aluminum foil (Al foil, 99.9%).

Synthesis of Ni-MOF

The previous synthesis method of Ni-MOF ($\{[H_2N(CH_3)_2]_2 [Ni_3(\mu_3\text{-}O)(XN)(BDC)_3]\cdot6DMF\}_n$) was referred to for this work, and some adjustments have been made.[33] In this solvent heat reaction, a mixture of NiCl$_2$·6H$_2$O (0.20 mmol, 0.0476 g), H$_2$BDC (0.20 mmol, 0.0332 g), XN (0.08 mmol, 0.0248 g), 8 mL DMF and 100 μL HNO$_3$ were added into a 23 mL Teflon-lined stainless vessel. The reaction vessel was then heated at 160 °C for 4 days and cooled to room temperature at 2 °C h^{-1} to collect the bright green hexagonal crystals. Subsequently, the product was then washed several times with DMF under sonication conditions. Finally, the sample was obtained through the filtration and drying process.

Syntheses of Li$^+$@Ni-MOF-X (X = 1, 2, and 3)

250 mg of the Ni-MOF sample was dispersed in 20 mL of a 0.5 M ethanol solution of LiNO$_3$ at room temperature. Respectively, the solution was changed three times per day for one, two and three days. Then, the Li$^+$@Ni-MOF samples that underwent lithium ion exchange treatment for different times were obtained and named as Li$^+$@Ni-MOF-1, Li$^+$@Ni-MOF-2, and Li$^+$@Ni-MOF-3, respectively. Subsequently, these samples were washed several times with anhydrous ethanol and filtered to dry naturally for 24 h.

Preparation of SSEs membranes

250 mg of the MOF sample was ground into a fine powder and homogeneously dispersed in the mixture solution of IPA and PTFE (MOF : PTFE = 9 : 1). The mixture was then rolled to form a flexible electrolyte film with a diameter of 16 mm and a thickness of about 300 μm. The membrane was vacuum dried at 80 °C for 12 h to remove excess solvent molecules. Then, the dried electrolyte film was transferred into an argon-filled glove box (H$_2$O ≤ 0.1 ppm, O$_2$ ≤ 0.1 ppm) and immersed in 1 M LiPF$_6$ solution for 24 h to adsorb a certain amount of Li$^+$. Finally, the electrolyte film was wiped with filter paper to remove excess liquid electrolyte and dried in an argon atmosphere.

Preparation of the cathode material LiFePO$_4$ (LFP)

LiFePO$_4$ (400 mg), AB (50 mg) and PVDF (50 mg) were mixed and ground with NMP (1.5 mL) to obtain the cathode mixture. Then, electrode films with a thickness of about 200 μm were prepared by applying the mixture on aluminium foils and drying at 120 °C for 10 h before cell fabrication. The mass of a single LiFePO$_4$ cathode material ranged from 0.0020 to 0.0050 g.

Morphology and structure characterization

Powder X-ray diffraction (PXRD) data were collected within a 2θ range of 5° to 50° using a PANalytical B. V. empirical diffractometer with Cu-Kα radiation. The scanning rate was 0.28° per second. Fourier transform infrared (FT-IR) spectra were obtained from 4000 to 400 cm^{-1} using a Bruker VERTEX70. Thermogravimetric analysis (TGA, PerkinElmer–STA 8000) was performed from 30 to 800 °C at a rate of 20 °C min^{-1} under a nitrogen atmosphere. The surface area and total pore volume were studied by the density functional theory (DFT, Quantachrome) method at 77 K from the nitrogen adsorption branch. The samples were degassed at 150 °C for 12 h before DFT measurements. The morphologies and structures of the MOFs materials were analysed by scanning electron microscopy (SEM, HITACHI S-4800). Determination of the nickel and lithium contents was employed by inductively coupled plasma-optical emission spectroscopy (ICP-OES, Agilent 725).

Electrochemical measurements

The σ of SSE placed between two stainless steel electrodes in a CR2032 coin cell was tested by alternating–current (AC) impedance spectroscopy. Measurements were performed using a CHI660E electrochemical workstation (Shanghai Chenhua Instrument Co., Ltd) with a frequency range of $1–10^5$ Hz, an amplitude of 5 mV, and a temperature range from 100 °C to −40 °C. The ionic conductivity (σ, S cm^{-1}) of the solid electrolyte was calculated using the following equation:

$$\sigma = \frac{l}{R_b S} \tag{1}$$

where R_b represents the body resistance, l represents the thickness, and S represents the contact area with the stainless steel.

The E_a was calculated using the Arrhenius equation as follows:

$$\sigma = Ae^{(-E_a/RT)} \tag{2}$$

where A and T are the apparent frequency factor and temperature, respectively.

The Li|SSE|Li symmetric cell was assembled and the t_{Li^+} was calculated according to Bruce Vincent's method as follows:

$$t_{Li^+} = \frac{I_s(\Delta V - I_0 R_0)}{I_0(\Delta V - I_s R_s)} \tag{3}$$

where R_0 and R_s denote the resistance before and after polarization, I_0 and I_s denote the initial and steady currents, respectively, and ΔV denotes the applied polarisation voltage (10 mV). The ESW of SSE in the asymmetric Li|SSE|Li cell was measured by linear scanning voltammetry (LSV) from 0 V to 7 V with a scan rate of 1 mV s^{-1}, respectively.

To monitor dendrite growth during lithium stripping/plating behavior in batteries, Li|SSE|Li symmetric batteries were tested for constant current charging and discharging at a current density of 0.1 mA cm^{-2} at room temperature. The LFP|SSE|Li cell also was assembled with LFP as cathode material, and its charge-discharge capacity and cycling ability further were studied at a current density of 0.1 C (1 C = 170 mA g^{-1}) between 2.5 and 4.2 V (LANDMon CT3004A).

# Results and discussion

Structural description of Ni-MOF

Ni-MOF, named as $\{[H_2N(CH_3)_2]_2 [Ni_3(\mu_3-O)(XN)(BDC)_3]\cdot 6DMF\}_n$, has been synthesized through a solvothermal method by referring to the literature.[33] The Ni-MOF possesses a unique anion framework with the $Me_2NH_2^+$ cations in the channels to maintain the charge balance of the three-dimensional (3D) anionic framework, providing convenient conditions for further lithium ion exchange. Moreover, this Ni-MOF presents a 3D triangular-bipyramidal cage cavity with a diameter of 11.8 Å, which not only can bring a special transmission pathway but also can provide a good jumping space for lithium-ion transport in the SSEs. Based on the structural characteristics of Ni-MOF, the sample was treated with 0.5 M LiNO$_3$ ethanol solution *via* an ion exchange strategy for 1, 2, and 3 days, and the resulting samples were named as Li$^+$@Ni-MOF-1, Li$^+$@Ni-MOF-2 and Li$^+$@Ni-MOF-3, respectively. $Me_2NH_2^+$ ions in Ni-MOF have been exchanged by Li$^+$, as schematically shown in Scheme 1.

ICP, PXRD, SEM, IR, TGA and N$_2$ Ads./Des. isotherms fundamental characterizations

The lithium contents in Li$^+$@Ni-MOF-1, Li$^+$@Ni-MOF-2 and Li$^+$@Ni-MOF-3 were determined by ICP−OES, as shown in Table S1. The experimental results showed that Li$^+$ was successfully exchanged with $Me_2NH_2^+$ in Ni-MOF, and the lithium content and molar ratio of Li to Ni increased with increasing exchange time. After two days of ion exchange, the ICP results showed a Li mass ratio of 0.071% (Li$^+$@Ni-MOF-1, 0.040%; Li$^+$@Ni-MOF-2, 0.133%) and a Li/Ni molar ratio of 0.0506 in Li$^+$@Ni-MOF-2.

PXRD tests have been carried out on the pristine Ni-MOF and the post-modified MOFs samples after the lithium ions exchange treatment for 1, 2 and 3 days. As shown in Fig. 1a, the positions and intensities of the diffraction peaks for experimental patterns were basically the same as that for the simulated ones, indicating that the prepared Ni-MOF possesses high phase purity. The structure of Ni-MOF still can maintain good stability after LiNO$_3$ treatment for different times.

In order to investigate the changes in the surface microscopic morphology of the Ni-MOF samples before and after ion exchange treatment by LiNO$_3$, scanning electron microscopy (SEM) was performed. As indicated in Fig. S1, the Ni-MOF and Li$^+$@Ni-MOF-2 samples present an octadecahedron morphology with six faces in the upper, lower and middle areas with high structural symmetry. The experimental results above are in good agreement with the previous reports
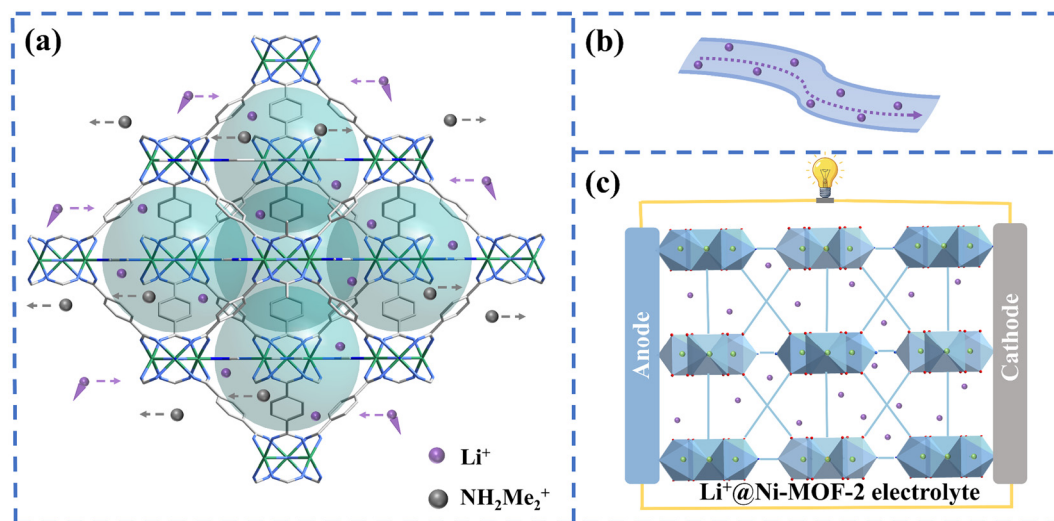
Scheme 1 Illustration of the structure (a) and the ion transport mechanism (b) for anionic Li⁺@Ni-MOF-2. (c) Application diagram of the Li⁺@Ni-MOF-2 electrolyte material in full cells.
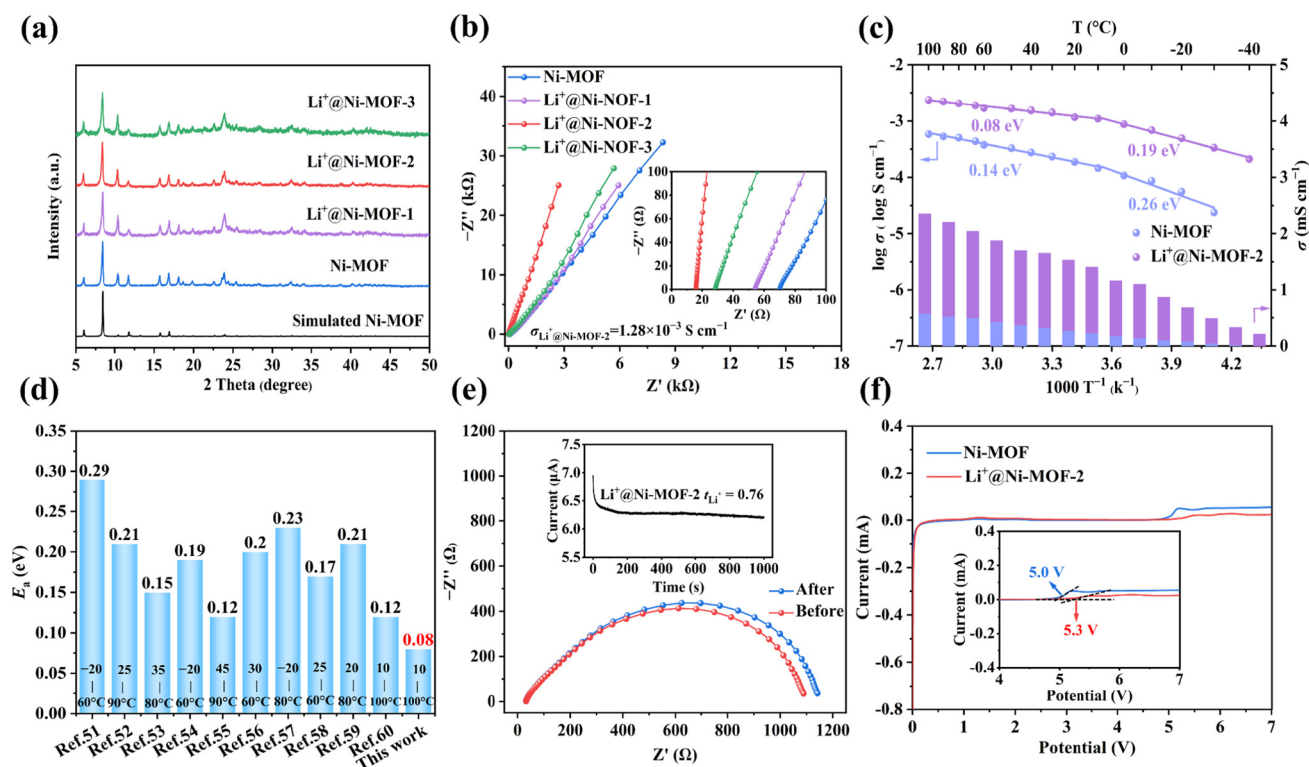
Fig. 1 (a) PXRD patterns of the simulated and synthesized samples of Ni-MOF, Li⁺@Ni-MOF-1, Li⁺@Ni-MOF-2 and Li⁺@Ni-MOF-3. (b) Nyquist plots of Ni-MOF, Li⁺@Ni-MOF-1, Li⁺@Ni-MOF-2, and Li⁺@Ni-MOF-3 at room temperature with impedance range from 0 to 18 kΩ (insert: the partial enlarged detail with impedance range from 0 to 100 Ω). (c) Arrhenius plots of Ni-MOF and Li⁺@Ni-MOF-2. (d) Summary of E_a of different SSEs. (e) EIS before and after polarization of Li|Li⁺@Ni-MOF-2|Li cells (the inset is the current−time curve). (f) LSV curves of Ni-MOF and Li⁺@Ni-MOF-2 SSEs with potential range from 0 to 7 V (insert: the partial enlarged detail with potential range from 4 to 7 V).

in the literature, demonstrating that Ni-MOF has no significant change in macrostructure after Li⁺ exchange treatment with good stability.[33]

Moreover, Ni-MOF and Li⁺@Ni-MOF-2 share similar FT-IR absorption peak positions, suggesting that there is no signifi-

cant disruption for the MOF structure before and after Li⁺ exchange (Fig. S2). The absorption peaks in the vicinity of 1737, 1399, and 742 cm⁻¹ can be attributed to the C═O, C═C, and Ni–O stretching vibrations, respectively.[34] Meanwhile, the Li⁺@Ni-MOF-2 material showed a characteristic peak of the Li–

O bond at 501 cm^{-1}, proving the successful exchange of Li$^+$.[35,36]

Notably, considering the safety issues, the good structural stability of MOF materials is of great importance in LMB applications. Hence, the TGA experiment was performed in the temperature range from 30 to 800 °C under nitrogen atmosphere to evaluate the thermal stability of Ni-MOF. As shown in Fig. S3, weight reductions of 33.49% were observed over the temperature range from 30 to 310 °C, which may be attributed to the removal of DMF molecules in the MOF samples mentioned above. Then, the MOFs skeletons started to gradually collapse after 360 °C. Importantly, the Li$^+$@Ni-MOF-2 SSE material almost can maintain its original morphology during different temperature ranges from 80 to 200 °C (80, 110, 140, 170, 185 and 200 °C) for 1 h (Fig. S4). This reveals the excellent interfacial thermal stability of Li$^+$@Ni-MOF-2 SSE, providing good stability support for the practical application of lithium ion batteries in the future.

To evaluate the influence of Li$^+$ exchange on the channels of the framework, the nitrogen adsorption/desorption isotherms of Ni-MOF and Li$^+$@Ni-MOF-2 have been investigated. As presented in Fig. S5 and Table S2, differences in the pore size, specific surface area and pore volume between Ni-MOF and Li$^+$@Ni-MOF-2 have been observed. DFT specific surface areas increased from the original 745.6 to 1009.8 m^2 g^{-1}, and the total pore volume increased from the original 0.318 to 0.462 cm^3 g^{-1}. From the above experimental results, the small-sized Li$^+$ (0.76 Å) replaces the large-sized Me$_2$NH$_2$$^+$ (6.64 Å) to expand the total pore volume, proving the successful exchange of ions.

Electrochemical performance

The σ values of the four prepared SSEs (Ni-MOF, Li$^+$@Ni-MOF-1, Li$^+$@Ni-MOF-2 and Li$^+$@Ni-MOF-3) have been evaluated and calculated by electrochemical impedance spectroscopy method (EIS). At room temperature, the different σ have been obtained for Ni-MOF, Li$^+$@Ni-MOF-1, Li$^+$@Ni-MOF-2 and Li$^+$@Ni-MOF-3 of 2.19 × 10^{-4}, 2.75 × 10^{-4}, 1.28 × 10^{-3} and 4.03 × 10^{-4} S cm^{-1}, respectively (Fig. 1b), suggesting that moderate Li$^+$ implantation may be better for Li$^+$ conduction. As the optimal sample, the Li$^+$@Ni-MOF-2 electrolyte achieved about an order of magnitude improvement in σ in comparison with that of the original Ni-MOF. Then, the σ were further determined for Ni-MOF and Li$^+$@Ni-MOF-2 over a wide temperature range from −40 to 100 °C. As shown in Fig. 1c and Table S3, the σ values rise gradually with the temperature increasing from −40 °C to 100 °C. For Ni-MOF, the σ values at 100 °C and −30 °C were 5.85 × 10^{-4} and 2.38 × 10^{-5} S cm^{-1}, respectively. Then, the Ni-MOF electrolyte was damaged at −40 °C. In comparison, Li$^+$@Ni-MOF-2 exhibits a better electrochemical performance with σ values of 2.36 × 10^{-3} S cm^{-1} at 100 °C and 2.12 × 10^{-4} S cm^{-1} at −40 °C, realizing the efficient applicability of the solid electrolyte over a wide temperature range. The excellent electrochemical performance of Li$^+$@Ni-MOF-2 may be attributed to the following three aspects: firstly, abundant Li$^+$ in the Ni-MOF framework is a key

factor for obtaining high σ, and the uniform distribution of Li$^+$ in the pores is conducive to the stable transport of Li$^+$;[24] Secondly, according to the single-ion hopping mechanism, Li$^+$ jumping on the anion framework may be beneficial to accelerate the ionic transport, further enhancing the electrochemical stability and interfacial contact between the Li$^+$@Ni-MOF-2 electrolyte and electrode.[32,37] Thirdly, the σ may be limited by the low concentration charge carrier with low Li$^+$ content of 0.040% for Li+@Ni-MOF-1.[38] The coulombic repulsion between Li$^+$ and other Li$^+$ may result in hindered migration at high Li$^+$ contents of 0.133% for Li$^+$@Ni-MOF-3. In comparison, the excellent σ of 1.28 × 10^{-3} S cm^{-1} at 25 °C can be reached with a medium Li$^+$ content of 0.071% for Li$^+$@Ni-MOF-2. Hence, a moderate concentration of Li$^+$ may be more conducive to the transmission of ions, which is consistent with previous reports.[39]

Unexpectedly, when the Li$^+$@Ni-MOF-2 was exposed to air for up to 140 days, it still remained stable (named as Li$^+$@Ni-MOF-2-140 d), presenting a high room temperature σ of 1.01 × 10^{-3} S cm^{-1} (Fig. S7 and Table S3). The σ value of Li$^+$@Ni-MOF-2 SSE is greater than that of SSEs that have been reported at room temperature or low temperature, as shown in Table S4.[40–49] Subsequently, fitting the obtained ionic conductivity-temperature relationship according to the Arrhenius equation yields E_a of 0.08 eV and 0.14 eV for Li$^+$@Ni-MOF-2, and 0.19 eV and 0.26 eV for the Ni-MOF electrolyte from 10 to 100 °C and −40 to 10 °C (Fig. 1c), respectively.

Actually, the σ of both Ni-MOF and Li$^+$@Ni-MOF-2 electrolytes show obvious differences at high and low temperatures. This may be attributed to EC with a low freezing point precipitating from the solvent as the temperature decreases, resulting in an increase in the electrolyte viscosity and further hindered migration of Li$^+$.[15,50,60] It is worth mentioning that the E_a of 0.08 eV for the Li$^+$@Ni-MOF-2 electrolyte is at a high level among the solid electrolytes reported so far. As presented in the detailed comparison (Fig. 1d and Table S5),[51–60] Huang et al.[51] embedded an anionic MOF-OH nanocage in a molten crystalline organic electrolyte (ML$_{20}$). The product MGM-MOF-OH with a continuous negative electrostatic environment and multimodal supramolecular interaction sites was obtained with an E_a of 0.29 eV. Zhang et al.[54] constructed a highly electronegative carboxyl-modified anionic MOF (InOF) that has a relatively low E_a (0.19 eV). Zheng et al.[56] developed SSE based on a three-dimensional interconnected MOF network (3D-PAN/PEO) with optimized pore size and strong cationic sites, presenting an E_a value of 0.20 eV. Liu et al.[60] introduced lauric acid as a moderator to obtain H-MIL-53-NH-SO$_3$Li with a hierarchical pore structure, obtaining a lower level of E_a (0.12 eV).

The experimental results above show that the effective exchange of Li$^+$ into the framework will facilitate an improvement in the electrochemical performance of the Li$^+$@Ni-MOF-2 electrolyte. Moreover, the t_{Li^+} should be investigated as an important parameter to evaluate ions transference in LMB SSEs. Then, the t_{Li^+} values of different SSEs were determined by applying a constant polarization voltage of 10 mV to the

assembled Li|SSE|Li cell through the Bruce–Vincent–Evans method. As indicated in Fig. 1e and Fig. S8, the t_{Li^+} of Ni-MOF before and after the ion exchange treatment were 0.57 for Ni-MOF and 0.76 for Li$^+$@Ni-MOF-2, respectively. This result indicates that the abundant transport concentration of Li$^+$ in the Li$^+$@Ni-MOF-2 pore channels plays an important role in enhancing t_{Li^+}.[61]

In order to evaluate the electrochemical stability of Ni-MOF and Li$^+$@Ni-MOF-2 SSEs, linear scanning voltammetry (LSV) has been employed to explore the ESW of the materials in the range from 0 to 7 V with a scanning rate of 1 mV s^{-1}. The results showed that the oxidative decomposition voltage of Ni-MOF is 5.0 V, while that of Li$^+$@Ni-MOF-2 ESW can be improved to 5.3 V (Fig. 1f), providing good stability support for the long-term stability cycling of the Li$^+$@Ni-MOF-2 electrolyte. A summary of the electrochemical properties can be viewed in Table 1. In comparison with the mainstream solid electrolytes reported, Li$^+$@Ni-MOF-2 also exhibits relatively higher t_{Li^+} and wider ESW (Table S6).

Cell performance

Li|Ni-MOF|Li and Li|Li$^+$@Ni-MOF-2|Li lithium symmetric batteries were assembled in order to investigate the long-term electrochemical dynamic stability and interfacial compatibility of SSEs with lithium metal. Firstly, constant-current lithium plating/stripping cycle tests were performed at a constant current density of 0.1 mA cm^{-2}. As shown in Fig. 2a, a short circuit phenomenon after 300 h of cycling has been observed with the overpotential up to 800 mV due to the rapid growth of lithium dendrites for the Ni-MOF electrolyte in the electrochemical reaction. Then, Ni-MOF shows an increasing trend of overpotential after 450 h. In contrast, the cell with Li$^+$@Ni-MOF-2 electrolyte possesses an initial overpotential of 140 mV, and it still can work normally with a stable overpotential of around 130 mV after 1000 h of cycling with a relatively smooth polarisation voltage curve (Fig. 2b).

Moreover, the surface morphology of lithium metal in cell after constant-current cycling with Ni-MOF and Li$^+$@Ni-MOF-2

Table 1 Summary of σ, E_a, t_{Li^+} and ESW of Ni-MOF, Li$^+$@Ni-MOF-2 and Li$^+$@Ni-MOF-2-140 d

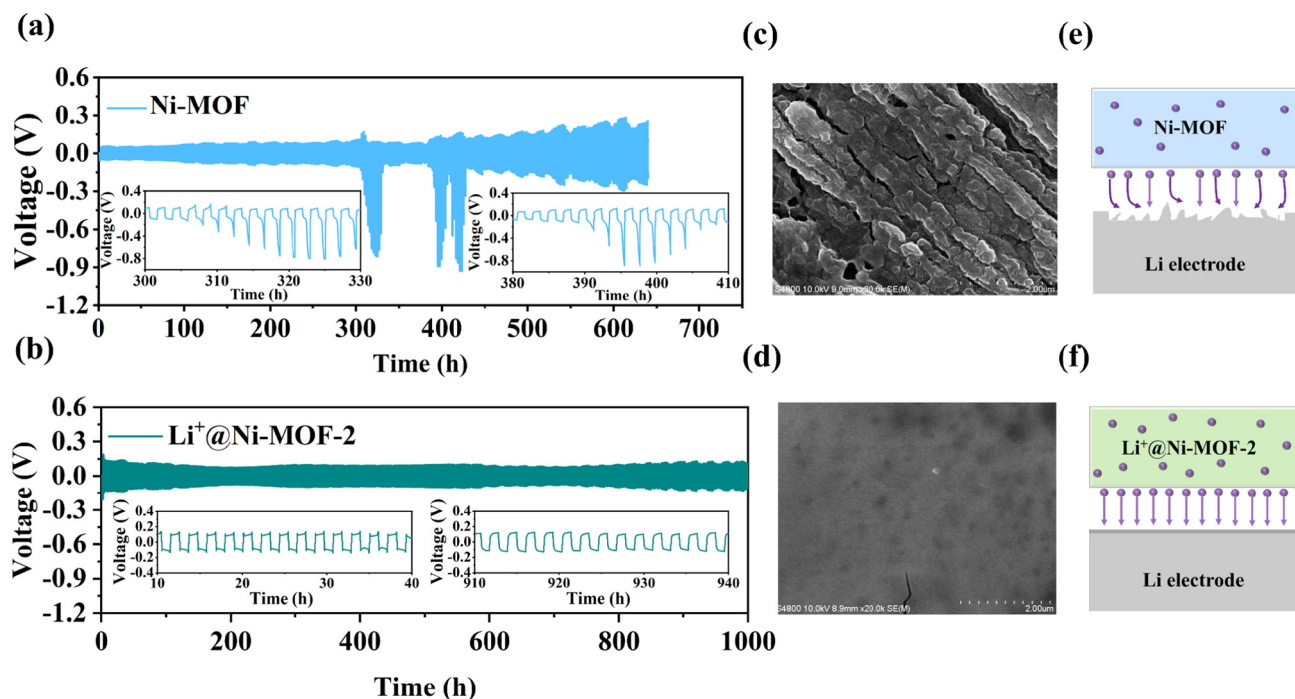| Samples	Ni-MOF	Li$^+$@Ni-MOF-2	Li$^+$@Ni-MOF-2-140 d
σ (S cm^{-1}, 100 °C)	5.85×10^{-4}	2.36×10^{-3}	2.57×10^{-3}
σ (S cm^{-1}, 25 °C)	2.19×10^{-4}	1.28×10^{-3}	1.01×10^{-3}
σ (S cm^{-1}, −40 °C)	—	2.12×10^{-4}	2.48×10^{-5}
E_a (eV, 10–100 °C)	0.14	0.08	—
t_{Li^+} (RT)	0.57	0.76	—
ESW (V, RT)	5.0	5.3	—

Fig. 2 (a) Voltage profile of the Li|Ni-MOF|Li symmetric cell at a current density of 0.1 mA cm^{-2} at room temperature from 0 to 800 h (inserts: the partial enlarged details with time range from 300 to 330 h (Left) and 380 to 410 h (Right)). (b) Voltage profile of the Li|Li$^+$@Ni-MOF-2|Li symmetric cell at a current density of 0.1 mA cm^{-2} at room temperature from 0 to 1000 h (inserts: the partial enlarged details with time range from 10 to 40 h (Left) and 910 to 940 h (Right)). The corresponding SEM images for the lithium foil surface of the Li symmetrical batteries with (c) Ni-MOF and (d) Li$^+$@Ni-MOF-2 electrolyte after lithium plating/stripping. Schematic of the Li deposition behavior with (e) Ni-MOF and (f) Li$^+$@Ni-MOF-2.

SSE as electrolytes was characterized in SEM analyses. Obviously, a very rough surface for the lithium electrode of the Ni-MOF cell can be observed, and a large number of cracks have been formed after constant current density cycling (Fig. 2c). On the contrary, the corresponding lithium metal in the Li$^+$@Ni-MOF-2 cell presents a relatively smooth surface under the same condition (Fig. 2d). The schematic diagrams of the Li deposition behavior are shown in Fig. 2e and f. The lithium deposition in the Ni-MOF cell may be attributed to the inhomogeneous Li$^+$ diffusion, further causing a short circuit in the battery. Obviously, the Li$^+$@Ni-MOF-2 electrolyte containing Li$^+$ is conducive to the improvement of the interfacial compatibility, which is beneficial to accelerate the Li$^+$ transport and the formation of a uniform interface.[62] Meanwhile, the dense lithium surface can inhibit the growth of lithium dendrites, exhibiting a better interfacial stability between the lithium metal electrode and electrolyte film.

In order to investigate the practical applicability of the prepared SSEs, full cells with the configuration LFP|Li$^+$@Ni-MOF-2|Li have been assembled and cycle-tested, where LFP serves as the cathode of the cell and lithium metal is the anode. The interfacial compatibility between Li$^+$@Ni-MOF-2 and the cathode material has been evaluated by the tests for the long-term cycling stability of the LFP|Li$^+$@Ni-MOF-2|Li cell at a corresponding current of 0.1 C. As presented in Fig. 3a and b, the initial discharge capacity of Li$^+$@Ni-MOF-2 is 158.03 mAh g^{-1}, which is close to the theoretical discharge capacity of 170 mAh g^{-1}. Then, the capacity retention still can reach 87.67% after 100 cycles, and the discharge capacity decreased to 128.48 mAh g^{-1} with 81.30% capacity retention after 150 cycles. At this point, the coulombic efficiency can still be as high as 98.49%. Notably, the average discharge capacity loss after each cycle is only 0.19% of the initial value, demonstrating the good cycling performance for the Li$^+$@Ni-MOF-2 electrolyte. With LFP as the cathode and Li$^+$@Ni-MOF-2 as the SSE, the assembled battery demonstrated good capacity retention rates after constant-current charge/discharge cycling (Table S7). The experimental results above are closely related to the formation of a good solid electrolyte interface during long-term cycling.

Then, the PXRD tests on Li$^+$@Ni-MOF-2 electrolytes after constant current charge/discharge cycling characterization were performed. As indicated in Fig. S9, compared to the original Ni-MOF sample, no significant change in the diffraction peak positions and peak intensity can be seen for the cycled Li$^+$@Ni-MOF-2 electrolytes, indicating their excellent electrochemical stability in the lithium battery working process.

The rate performance of Li$^+$@Ni-MOF-2 SSE has been tested for different magnifications at room temperature at currents
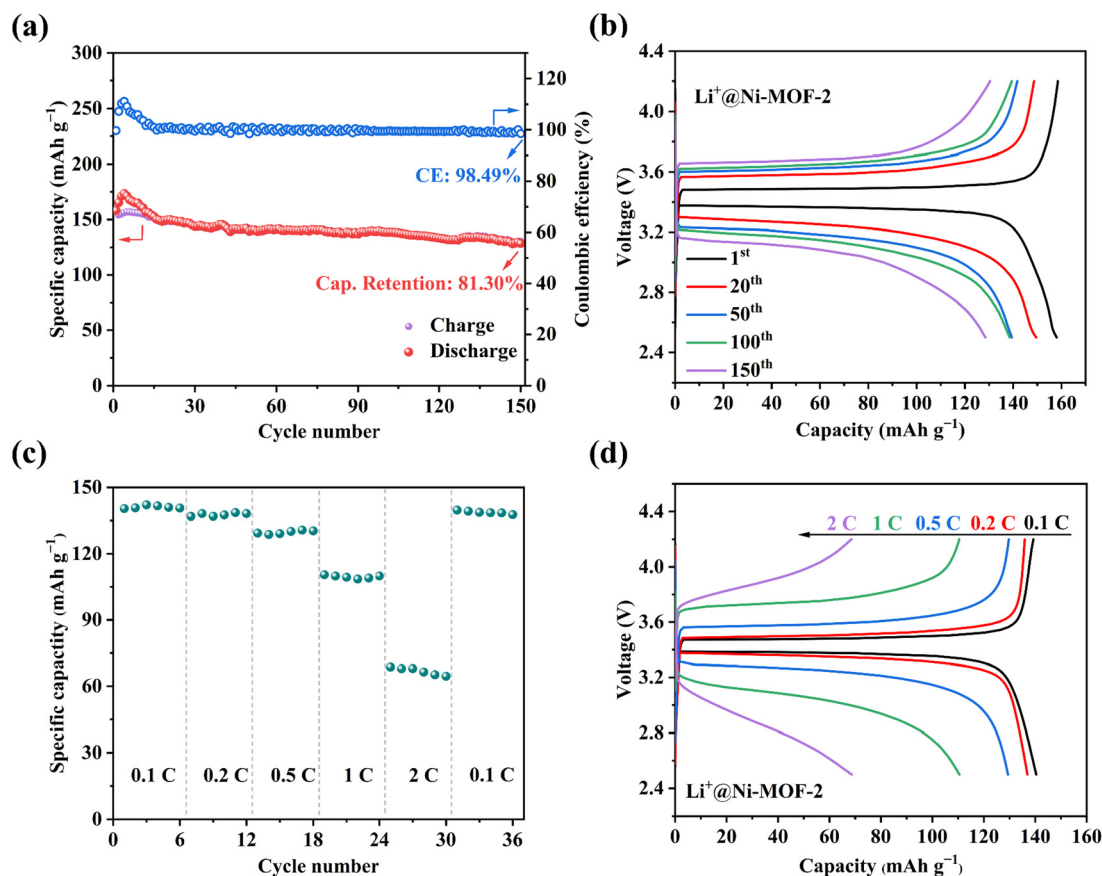

Fig. 3 (a) Charge/discharge capacity and coulombic efficiency of Li$^+$@Ni-MOF-2. (b) Charge/discharge cycling curves of Li$^+$@Ni-MOF-2 at 0.1 C. (c) Rate performance of Li$^+$@Ni-MOF-2 SSEs. (d) Charge and discharge voltage profiles of Li$^+$@Ni-MOF-2 at different rates.

Fig. 4 Photographs of the bulbs lit by LFP|Li$^+$@Ni-MOF|Li cells at different temperatures: (a) RT, (b) −20 °C, (c) −30 °C, (d) −40 °C, (e) and (f) −45 °C, (g) 30 °C, and (h) 25 °C.

corresponding to 0.1, 0.2, 0.5, 1.0, and 2.0 C (1 C = 170 mA g^{-1}) (Fig. 3c and d). The Li$^+$@Ni-MOF-2 cell discharge capacity was 140.11, 136.94, 129.41, 110.52, and 68.65 mAh g^{-1}, respectively. In particular, the discharge capacity of the LFP|Li$^+$@Ni-MOF-2|Li cell recovered to 139.71 mAh g^{-1} after several cycles when the current was adjusted to 0.1 C, which is comparable to the initial discharge capacity, indicating the excellent multiplicity performance of the Li$^+$@Ni-MOF-2 electrolyte.

Actually, good electrochemical properties for SSEs at low temperatures play a key role in the practical application. Thus, the low-temperature performance of Li$^+$@Ni-MOF-2 was studied in detail. Firstly, two LFP|Li$^+$@Ni-MOF-2|Li full cells were assembled and mounted on the LED devices, and sequentially exposed to different temperature environments (room temperature (RT), −20 °C, −30 °C, −40 °C, −45 °C, 30° C and 25 °C) (Fig. 4). Then, the bulbs were lit with different brightness. The bulb became brighter with higher temperature, which is attributed to temperature decreases causing an increase of the resistance in the electrolyte. In addition, with the increasing voltage drop as the current passes through the bulb, there is a lower actual voltage output to the bulb, resulting in a decrease in brightness. Notably, the LED bulb can be lit for at least 8 minutes at −45 °C, which indicates that the Li$^+$@Ni-MOF-2 solid-state electrolyte still has good electrochemical performance and stability under an ultra-low temperature environment, featuring its good potential in practical application.

Conclusions

In summary, a cation-exchange strategy between Li$^+$ and $(CH_3)_2NH_2^+$ was employed for developing an anionic Ni-MOF SSE. The abundant free lithium ions in the MOF pores significantly enhanced the electrochemical performance of the SSE. In comparison with the original Ni-MOF, the Li$^+$@Ni-MOF-2 electrolyte revealed obvious electrochemical performance improvement, presenting a σ value of 1.28 × 10^{-3} S cm^{-1} at 25 °C and 2.36 × 10^{-3} S cm^{-1} at 100 °C, E_a of 0.08 eV from 10 to 100 °C, t_{Li^+} of 0.76 and ESW of 5.3 V. Importantly, it still retained the σ

value of 2.12 × 10^{-4} S cm^{-1} at an ultra-low temperature (−40 °C) and was employed to keep LED lights on continuously at −45 °C. Moreover, LFP|Li$^+$@Ni-MOF-2|Li full cells with the first discharge capacity of 158.03 mAh g^{-1} stably cycled for 150 cycles at a current density of 0.1 C with a capacity retention of 81.30%. This ion-exchange method has achieved an effective balance and improvement among the key electrochemical properties, providing the possibility for the efficient operation of batteries within a wide temperature range.

Author contributions

The manuscript was written with contributions from all authors. All authors have approved of the final version of the manuscript.

Conflicts of interest

There are no conflicts to declare.

Data availability

All the data needed to evaluate this work are available in the main manuscript and/or the SI.

The contents of the SI file includes PXRD pattern, SEM images, FT-IR spectra, TGA, N$_2$ Ads./Des. isotherms, ICP and other electrochemical test data. See DOI: https://doi.org/10.1039/d5dt01485a.

Acknowledgements

References

1 R. Pathak, K. Chen, F. Wu, A. U. Mane, R. V. Bugga, J. W. Elam, Q. Qiao and Y. Zhou, *Energy Storage Mater.*, 2021, **41**, 448–465.

2 X. Wang, Z. Chen, K. Jiang, M. H. Chen and S. Passerini, *Adv. Energy Mater.*, 2024, **14**, 2304229.

3 Y. X. Zhong, X. Y. Yang, R. Q. Guo, L. Q. Zhai, X. R. Wang, F. Wu, C. Wu and Y. Bai, *Electrochem. Energy Rev.*, 2024, **7**, 30.

4 Z. X. Huang, Z. C. Xiao, R. S. Jin, Z. Li, C. Y. Shu, R. Y. Shi, X. W. Wang, Z. X. Tang, W. Tang and Y. P. Wu, *Energy Environ. Sci.*, 2024, **17**, 5365–5386.

5 Y. T. Liu, Y. Elias, J. S. Meng, D. Aurbach, R. Q. Zou, D. G. Xia and Q. Q. Pang, *Joule*, 2021, **5**, 2323–2364.

6 B. Hennequart, M. Platonova, R. Chometon, T. Marchandier, A. Benedetto, E. Quemin, R. Dugas, C. Lethien and J. M. Tarascon, *ACS Energy Lett.*, 2024, **9**, 454–460.

7 S. J. Liu, L. Zhou, T. J. Zhong, X. Wu and K. Neyts, *Adv. Energy Mater.*, 2024, **14**, 2403602.

8 J. Park, H. Seong, C. Yuk, D. Lee, Y. Byun, E. Lee, W. Lee and B. J. Kim, *Adv. Mater.*, 2024, **36**, 2403191.

9 K. Jun, Y. Chen, G. Wei, X. C. Yang and G. Ceder, *Nat. Rev. Mater.*, 2024, **9**, 887–905.

10 N. N. Zhang, Q. S. He, L. Zhang, J. Zhang, L. F. Huang and X. Y. Yao, *Adv. Mater.*, 2024, **36**, 2408903.

11 X. Y. Ji, Y. R. Zhang, M. X. Cao, Q. C. Gu, H. L. Wang, J. S. Yu, Z. H. Guo and X. G. Zhou, *J. Adv. Ceram.*, 2022, **11**, 835–861.

12 J. J. Lu, B. F. Sheng, M. F. Chen, M. Xu, Y. Y. Zhang, S. Zhao, Q. Q. Zhou, C. Y. Li, B. Wang, J. J. Liu, J. Z. Chen, Z. C. Lou and X. Han, *Energy Storage Mater.*, 2024, **71**, 103570.

13 S. Z. Cong, Y. Q. Zhou, C. L. Luo, C. X. Wang, J. X. Wang, Z. Wang and X. L. Liu, *Angew. Chem., Int. Ed.*, 2024, **63**, e202319894.

14 I. E. Khalil, J. Fonseca, M. R. Reithofer, T. Eder and J. M. Chin, *Coord. Chem. Rev.*, 2023, **481**, 215043.

15 X. Wang, S. Jin, L. Shi, N. Zhang, J. Guo, D. Q. Zhang and Z. L. Liu, *ACS Appl. Mater. Interfaces*, 2024, **16**, 33954–33962.

16 K. Wang, Z. Y. Li, Y. Peng, T. F. Zheng, J. L. Chen, S. J. Liu and H. R. Wen, *Inorg. Chem.*, 2023, **62**, 17993–18001.

17 M. M. Wang, T. Z. Xiong, B. C. Chen, J. J. Hu, H. R. Wen and S. J. Liu, *Inorg. Chem.*, 2023, **62**, 21322–21328.

18 X. N. Zhang, B. C. Chen, J. L. Zhang, J. L. Zhang, S. J. Liu and H. R. Wen, *Dalton Trans.*, 2022, **51**, 15762–15770.

19 X. D. Zhang, W. Y. Ding, C. B. Jiao, X. X. Kang and Z. L. Liu, *Inorg. Chem.*, 2024, **63**, 3383–3392.

20 W. Y. Ding, H. B. Tai, X. Y. Tang, D. W. Xu, S. Jin, X. M. Kang and Z. L. Liu, *Appl. Catal., B*, 2025, **361**, 124685.

21 H. B. Tai, W. Y. Ding, X. Zhang, K. C. Liang, Y. Rong and Z. L. Liu, *Inorg. Chem.*, 2024, **63**, 18083–18091.

22 Y. Peng, H. T. Xiong, P. X. Zhang, Z. W. Zhao, X. Liu, S. H. Tang, Y. Liu, Z. L. Zhu, W. Z. Zhou, Z. N. Deng, J. H. Liu, Y. Zhong, Z. L. Wu, J. W. Chen, Z. Y. Zhou, S. X. Chen, S. G. Deng and J. Wang, *Nat. Commun.*, 2024, **15**, 625.

23 X. L. Wang, X. Zhang, A. N. He, J. Guo and Z. L. Liu, *Inorg. Chem.*, 2024, **63**, 6948–6956.

24 F. C. Tao, X. Wang, S. Jin, L. Tian, Z. X. Liu, X. M. Kang and Z. L. Liu, *Adv. Mater.*, 2023, **35**, 2300687.

25 D. D. Han, P. F. Wang, P. Li, J. Shi, J. Liu, P. J. Chen, L. P. Zhai, L. W. Mi and Y. Z. Fu, *ACS Appl. Mater. Interfaces*, 2021, **13**, 52688–52696.

26 X. Wang, L. Tian, F. C. Tao, M. Y. Liu, S. Jin and Z. L. Liu, *Dalton Trans.*, 2023, **52**, 10222–10230.

27 J. L. Jiang, R. H. Zhang, J. C. Guo, S. Q. Zhang, X. T. Min, Z. Y. Liu, N. Liu, D. Cao, J. Xu, P. Cheng and W. Shi, *Nano Lett.*, 2025, **25**, 3781–3790.

28 Q. Q. Li, Y. Yan, Z. W. Jiang, T. H. Chen and Q. W. Li, *Inorg. Chem.*, 2024, **63**, 10585–10593.

29 H. Jiang, Y. Q. Du, L. Y. Zhao, X. Y. Liu, J. R. Kong, P. Liu and T. Zhou, *Chem. Eng. J.*, 2024, **487**, 150455.

30 L. Shen, H. B. Wu, F. Liu, J. L. Brosmer, G. Shen, X. F. Wang, J. I. Zink, Q. F. Xiao, M. Cai, G. Wang, Y. F. Lu and B. Dunn, *Adv. Mater.*, 2018, **30**, 1707476.

31 Y. Ouyang, W. Gong, Q. Zhang, J. Wang, S. J. Guo, Y. B. Xiao, D. X. Li, C. H. Wang, X. L. Sun, C. Y. Wang and S. M. Huang, *Adv. Mater.*, 2023, **35**, 2304685.

32 R. A. Kharod, J. L. Andrews and M. Dincă, *Annu. Rev. Mater. Res.*, 2022, **52**, 103–128.

33 X. M. Kang, Z. Q. Wang, X. L. Shi, X. L. Jiang, Z. L. Liu and B. Zhao, *Small*, 2024, **20**, 2311511.

34 W. F. Zhai, Y. Chen, Y. D. Liu, T. Sakthivel, Y. Ma, Y. B. Qin, Y. Q. Qu and Z. F. Dai, *ACS Nano*, 2023, **17**, 17254–17264.

35 K. Zaghib, A. A. Salah, N. Ravet, A. Mauger, F. Gendron and C. M. Julien, *J. Power Sources*, 2006, **160**, 1381–1386.

36 L. Tian, X. B. Xu, M. Y. Liu, Z. X. Liu and Z. L. Liu, *Langmuir*, 2021, **37**, 3922–3928.

37 X. Li, Q. Hou, W. Huang, H. S. Xu, X. W. Wang, W. Yu, R. L. Li, K. Zhang, L. Wang, Z. X. Chen, K. Y. Xie and K. P. Loh, *ACS Energy Lett.*, 2020, **5**, 3498–3506.

38 W. W. Deng, X. Li, W. B. Shi, Q. J. Liu, J. Y. Jiang and X. Y. Feng, *J. Alloys Compd.*, 2020, **843**, 155942.

39 S. H. Yang, S. Y. Kim and G. Y. Chen, *ACS Energy Lett.*, 2024, **9**, 2212–2221.

40 W. C. He, D. X. Li, S. J. Guo, Y. B. Xiao, W. Gong, Q. H. Zeng, Y. Ouyang, X. Li, H. Y. Deng, C. Tan, Q. Zhang and S. M. Huang, *Energy Storage Mater.*, 2022, **47**, 271–278.

41 S. X. Liu, G. S. Jiang, Y. M. Wang, C. Y. Liu, T. Y. Zhang, Y. Y. Wei and B. G. An, *ACS Nano*, 2024, **18**, 14907–14916.

42 J. Guo, X. Wang, L. Shi and Z. L. Liu, *Chem. Commun.*, 2025, **61**, 2103–2106.

43 Y. F. Zhang, J. J. Huang, H. Liu, W. J. Kou, Y. Dai, W. Dang, W. J. Wu, J. T. Wang, Y. Z. Fu and Z. Y. Jiang, *Adv. Energy Mater.*, 2023, **13**, 2300156.

44 J. Li, Y. J. Cai, Y. Y. Cui, H. Wu, H. R. Da, Y. J. Yang, H. T. Zhang and S. J. Zhang, *Nano Energy*, 2022, **95**, 107027.

45 L. Tian, Z. X. Liu, F. C. Tao, M. Y. Liu and Z. L. Liu, *Dalton Trans.*, 2021, **50**, 13877–13882.

46 Z. Q. Wang, R. Tan, H. B. Wang, L. Y. Yang, J. T. Hu, H. B. Chen and F. Pan, *Adv. Mater.*, 2018, **30**, 1704436.

47 Y. F. Xuan, Y. X. Wang, B. Y. He, S. Y. Bian, J. C. Liu, B. Q. Xu and G. Zhang, *Chem. Mater.*, 2022, **34**, 9104–9110.

48 Q. Zhang, D. X. Li, J. Wang, S. J. Guo, W. Zhang, D. Chen, Q. Li, X. H. Rui, L. Y. Gan and S. M. Huang, *Nanoscale*, 2020, **12**, 6976–6982.

49 X. Y. Huang, S. Huang, T. Y. Wang, L. Zhong, D. M. Han, M. Xiao, S. J. Wang and Y. Z. Meng, *Adv. Funct. Mater.*, 2023, **33**, 2300683.

50 R. Zettl, S. Lunghammer, B. Gadermaier, A. Boulaoued, P. Johansson, H. M. R. Wilkening and I. Hanzu, *Adv. Energy Mater.*, 2021, **11**, 2003542.

51 Y. F. Xie, L. L. Xu, Y. Tong, Y. Ouyang, Q. H. Zeng, D. X. Li, Y. B. Xiao, S. T. Yu, X. L. Liu, C. Zheng, Q. Zhang and S. M. Huang, *Adv. Mater.*, 2024, **36**, 2401284.

52 H. Yang, B. T. Liu, J. Bright, S. Kasani, J. H. Yang, X. W. Zhang and N. Q. Wu, *ACS Appl. Energ. Mater.*, 2020, **3**, 4007–4013.

53 Q. C. Xia, K. X. Han, X. X. Ma, P. T. Qiu, Z. Y. Li and X. N. Chen, *Chem. Sci.*, 2024, **15**, 17579–17589.

54 X. Duan, Y. Ouyang, Q. H. Zeng, S. Y. Ma, Z. Kong, A. Chen, Z. W. He, T. Yang and Q. Zhang, *Inorg. Chem.*, 2021, **60**, 11032–11037.

55 T. Wang, H. Yuan, H. M. Wang, Y. Guo, J. Yang, X. M. Liu, B. B. Liu, X. Y. Wang, C. H. Kirk, J. G. Sun, Y. W. Zhang and J. Wang, *Adv. Funct. Mater.*, 2024, **34**, 2405699.

56 Z. L. Li, S. X. Wang, J. K. Shi, Y. Liu, S. Y. Zheng, H. Q. Zou, Y. L. Chen, W. X. Kuang, K. Ding, L. Y. Chen, Y. Q. Lan, Y. P. Cai and Q. F. Zheng, *Energy Storage Mater.*, 2022, **47**, 262–270.

57 M. Yao, T. H. Yu, Q. Q. Ruan, Q. J. Chen, H. T. Zhang and S. J. Zhang, *ACS Appl. Mater. Interfaces*, 2021, **13**, 47163–47173.

58 Y. Zheng, N. Yang, R. Gao, Z. Q. Li, H. Z. Dou, G. R. Li, L. T. Qian, Y. P. Deng, J. Q. Liang, L. X. Yang, Y. Z. Liu, Q. Y. Ma, D. Luo, N. Zhu, K. C. Li, X. Wang and Z. W. Chen, *Adv. Mater.*, 2022, **34**, 2203417.

59 Z. W. Lei, J. L. Shen, J. Wang, Q. Qiu, G. Z. Zhang, S. S. Chi, H. L. Xu, S. Li, W. D. Zhang, Y. S. Zhao, Y. H. Deng and C. Y. Wang, *Chem. Eng. J.*, 2021, **412**, 128733.

60 X. Wang, S. Jin, L. Shi, N. Zhang, J. Guo, D. Q. Zhang and Z. L. Liu, *Small Methods*, 2025, **9**, 2400968.

61 W. T. Xu, X. K. Pei, C. S. Diercks, H. Lyu, Z. Ji and O. M. Yaghi, *J. Am. Chem. Soc.*, 2019, **141**, 17522–17526.

62 N. Chen, Y. J. Li, Y. J. Dai, W. J. Qu, Y. Xing, Y. S. Ye, Z. Y. Wen, C. Guo, F. Wu and R. J. Chen, *J. Mater. Chem. A*, 2019, **7**, 9530–9536.